Journal of Materials Chemistry C

ROYAL SOCIETY OF CHEMISTRY

PAPER

View Article Online
View Journal

Cite this: DOI: 10.1039/d5tc03674g

ZnO-free organic solar cells with a self-assembled monolayer as an ETL for improved stability

Chélia Zalani,[a] Gilles H. Roche,[a] Olivier J. Dautel,[b] Martial Leyney,[a] Jean-Sébastien Filhol,[b] Roland Lefèvre,[c] Christine Labrugère-Sarroste,[d] Gilles Pécastaings,[e] Guillaume Wantz[a] and Sylvain Chambon*[a]

Despite constant improvements in the performance, the stability of organic photovoltaic (OPV) solar cells remains hindered. One of the limiting factors is the degradation happening at the interface between the metal oxide electron transport layer (ETL) and the organic active layer. In particular, well known zinc oxide (ZnO) exhibits photocatalytic activity that degrades organic materials, resulting in an altered interface, ultimately affecting the performance upon operation. As a means to address this issue, the use of self-assembled monolayers (SAM) in replacements of ZnO is investigated. Here, we design and synthetize a molecule, **2PAP-SAM**, ensuring a favourable molecular dipole, ensuring a suitable shift of the work function from 5.16 eV for pristine cleaned ITO to 4.34 eV after SAM functionalisation. This shift contributes to a better energy level alignment between the cathode and the LUMO level of the acceptor molecule. Solar cells with **PTQ10**:**Y6** as an active layer were then fabricated with **2PAP-SAM** as an ETL, and compared to a reference device with ZnO. Devices with the SAM exhibited power conversion efficiencies (PCEs) reaching up to 10%, with a V_{OC} of around 0.78 V, close to the reference devices made with ZnO, which exhibited a PCE of 11% with a V_{OC} of 0.81 V. In comparison, devices without any ETL show only poor performances. Furthermore, stability studies under continuous light illumination were performed and showed that devices with the SAM as an ETL exhibit improved stability compared to devices with ZnO.

Received 10th October 2025,
Accepted 12th February 2026

DOI: 10.1039/d5tc03674g

rsc.li/materials-c

1. Introduction

Organic photovoltaic (OPV) technology is a promising emergent photovoltaic technology that is characterised by its use of organic semiconductors as photoactive main materials. These materials allow both the precise tuning of the bandgap of interest and the creation of flexible, semi-transparent, and light weight modules with low overall energy pay-back time thanks to low temperatures and printing processes.[1,2] The performance of OPV cells has steadily improved over recent years,[3–5] and notably, a symbolic power conversion efficiency (PCE) of 20% was recently achieved for a single junction in a laboratory, due to improvement and control of active layer materials and morphology,[6,7] and a PCE of 14.5% was achieved in modules of 204 cm^2.[8,9]

Nonetheless, one of the major drawbacks of the current state of the technology is the limited lifetime of devices resulting from many intrinsic and extrinsic degradation processes.[10–12] A first step towards more stable cells was moving to an inverted (n–i–p) architecture to prevent the use of a low work function metal on top of the device that can be oxidised by the ambient environment with deteriorating performance during use.[13,14] Still, the architecture was developed with the use of a metal oxide as a charge transport interlayer that can interact with the organic active materials. One well known example of this intrinsic process is the deterioration upon ageing caused by the photocatalytic activity of zinc oxide (ZnO) used as an electron transport material (ETL).[12,15–21] Additionally, ZnO requires UV light activation to act as a good ETL material,[20] which is problematic, with the use of UV-filters on the OPV to minimize active material degradation. As such, other strategies can be implemented, and among them is the use of self-assembled monolayers (SAM). This concept involves either functionalizing the ZnO layer with small molecules that can selectively bind with the metal oxide, or totally replacing ZnO with a SAM with at least comparable charge extraction capabilities. The first approach has been developed with **IC-SAM** (Fig. 1b),[22,23] with successful integration in devices and passivation of the ZnO layer, even leading to a predicted lifetime of 30 years with the addition of a buffer layer between the hole transport layer (HTL)

[a] Univ. Bordeaux, CNRS, Bordeaux INP, IMS, UMR 5218, F-33400 Talence, France. E-mail: sylvain.chambon@ims-bordeaux.fr
[b] Institut Charles Gerhardt de Montpellier, CNRS, UM, ENSCM, UMR 5253, 34283 Montpellier, France
[c] Univ. Bordeaux, CNRS, Bordeaux INP, LCPO, UMR 5629, F-33600 Pessac, France
[d] Univ. Bordeaux, CNRS, PLACAMAT, UAR 3626, F-33600 Pessac, France
[e] Univ. Bordeaux, CNRS, Bordeaux INP, CRPP, UMR 5031, F-33600 Pessac, France

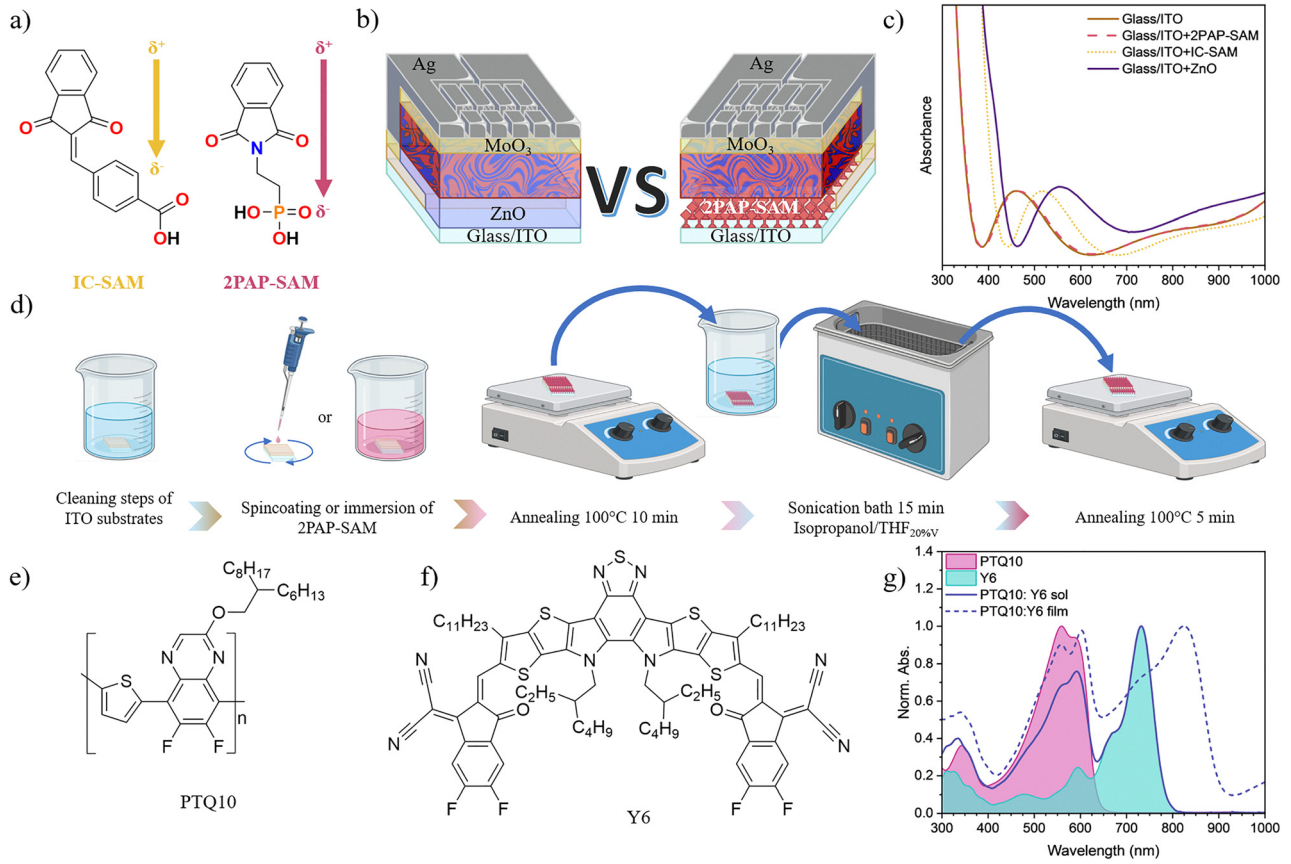

Fig. 1 (a) Chemical structure of **IC-SAM** and **2PAP-SAM** with molecular dipoles shown, (b) inverted architecture of an organic solar cell with ZnO and SAM as the ETL, (c) absorbance of the ITO substrate with SAMs and ZnO, (d) schematic representation of the deposition of the SAM onto ITO, (e) chemical structure of the active material **PTQ10**, (f) chemical structure of the active material **Y6**, and (g) normalised absorbance spectra of pristine materials in solution and of the blend in solution and in a film.

and active layer.[24] However, for the second strategy, most of the work focusing on replacing layers by SAMs was carried out to get rid of the HTL in the direct (p–i–n) architecture, especially with the now well-known 2PACz family used in perovskite solar cells[25–27] and later by the OPV community.[28–31]

Concerning the use of a SAM as an ETL, only a few reports have been published. Recently, Jeong *et al.* demonstrated that the "ZnO-free" device strategy for an inverted architecture can be effectively implemented with the high performance material D18:**Y6**, surpassing even the reference devices made of ZnO as an ETL with a PCE of 17.53%, putting in context the importance of an interfacial molecular dipole, while focusing on mechanical stability for flexible application.[32] However, no report has been published on the potential improvement of the stability upon operation with a SAM ETL. Therefore, it is important to focus on investigating the potential of using SAM molecules to improve the operational stability under light of inverted organic photovoltaic devices. To this aim, the molecule has to be tailored to optimize the molecular dipole, work function, and surface energy, in order to act as an electron transport layer in inverted solar cells by fully replacing the ZnO layer to minimize degradation mechanisms. An anchoring group is also necessary to covalently bind to the transparent conductive electrode, which is generally indium tin oxide (ITO). Several chemical functionalities are possible, and among them phosphonic acids (PAs) present numerous advantages. In contrast to silane end groups, PAs offer easier synthesis, purification and storage capacity, since they don't undergo self-condensation. Compared to carboxylic acids, they allow stronger and easier binding with the metal oxide.[33,34] They also present a large variety of binding modes in the presence of three oxygen, allowing two slightly different binding mechanisms with weaker or stronger Lewis acid metal oxides. For ITO, the weaker Lewis acid mechanism, strengthened by UV-O_3 pre-surface treatment, is generally preferred, since it both allows a thorough sample surface cleaning procedure to be retained, and the promotion of more homogenous binding of PAs.

In this work, we introduce a SAM called **2PAP-SAM** (Fig. 1b), which was designed and synthesised using an electron deficient phthalimide group on one end, in order to form a suitable dipole with a negative barycentre being closer to ITO, and a phosphonic acid as an anchoring group on the other end. We explored and optimised the grafting procedure on the ITO substrate. The functionalised ITO electrode with **2PAP-SAM** was thoroughly characterised by several means to confirm the efficient grafting and modification of the electrode work

function. **2PAP-SAM** was then introduced as an ETL in inverted organic solar cell (OSC) devices with **PTQ10** and **Y6** (Fig. 1e and f) as active materials, and compared to ZnO reference cells and **IC-SAM** as other ETL candidates with the full architecture illustrated in Fig. 1a. The absorbances of the materials are displayed in Fig. 1c and g and Fig. S7. Performances close to that of the ZnO device have been reached with **2PAP-SAM**. Stability studies were thereafter performed and showed that such ZnO-free cells reduce the degradation of the OSC devices by suppressing the alteration at the interface between the active layer and the ETL.

2. Results and discussion

2.1. Synthesis of 2PAP-SAM

2PAP-SAM was obtained in one step by dealkylation of commercially available **Et_2PAP** using 3 equivalents of Me_3SiBr in dry dichloromethane over 22 h at room temperature (Fig. 3). The crude product was submitted to recrystallization in toluene to offer **2PAP-SAM** as a white solid with a yield of 87%. The experimental procedure and characterization have been added to the SI.

DFT calculations at the PBE + D3 level have also been conducted to obtain the molecular dipole of **2PAP-SAM** and compare it to **IC-SAM** calculation and the literature value of 1.92 D.[22] In this work, the **IC-SAM** molecular dipole was calculated at 2.07 and 3.36 D, depending on the proton position on the carboxylic moiety, for an energy difference between the two isomers below k_BT (Fig. S13). This suggests that a proton exchange is happening between the two sites leading to a dipole moment larger than the one previously computed. The **2PAP-SAM** values of the molecular dipole were computed to 3.35 and 5.11 D depending on the position of the hydrogen on the phosphonic moiety, with the isomer with the lowest dipole moment being $3k_BT$ more stable than the other one leading to an average dipole moment of 3.5 D, larger than that of **IC-SAM**, as illustrated in Fig. 1b.

2.2. Surface functionalisation of ITO by 2PAP-SAM

First, the functionalisation of ITO by **2PAP-SAM** was investigated as well as its possible impact on the ITO work function (WF). Two methods for functionalising the substrates were studied, immersion and spincoating, as illustrated in Fig. 1d.

In the case of immersion, ITO substrates were dipped in 1 mM **2PAP-SAM** THF solution and in THF control solution for different times, then underwent 10 min of annealing at 100 °C to facilitate chemical bonding, and were rinsed thoroughly to remove excess unbonded molecules (see Experimental section for details). The samples were then first characterised by Kelvin probe (KP) measurement to follow the change in the WF. Fig. 2a and Table S1 show that for ITO substrates functionalised by immersion, starting with 1 h of treatment, a favourable and significant shift of the work function from 5.16 eV for pristine UV-O_3 cleaned ITO to 4.46 eV is observed, and an ideal 4.23 eV work function was obtained after 24 h of immersion. This shift allows a better energetic level alignment with the **Y6** acceptor

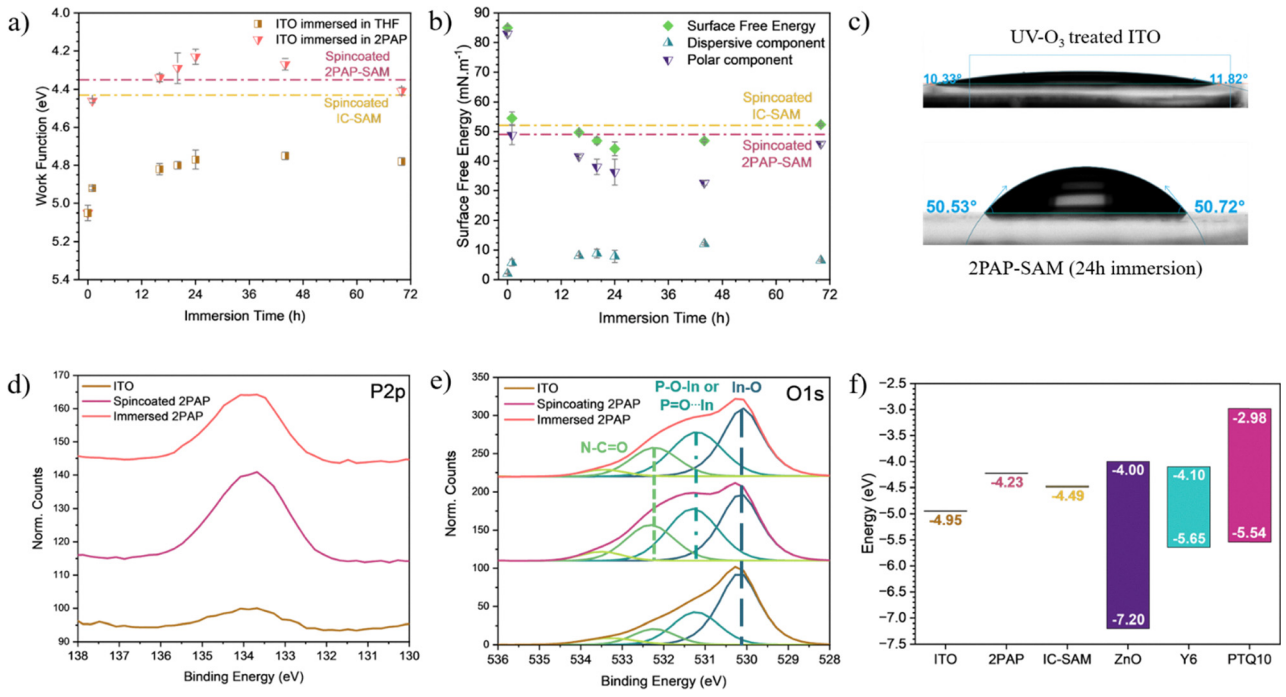

Fig. 2 (a) Evolution of the work function and (b) surface free energy for ITO immersed in **2PAP-SAM** and the control solution, (c) picture of contact angle measurement with water for ITO after UV-O_3 treatment and immersion in **2PAP-SAM** solution, XPS measurement for (d) P2p and (e) O1s orbitals with deconvolution, and (f) Fermi level of ITO and ITO + SAM derived from KP measurement. The energy level of ZnO is derived from UPS and UV-visible measurement and the energy level of the active materials is calculated using cyclic voltammetry results from the literature.[34,35]

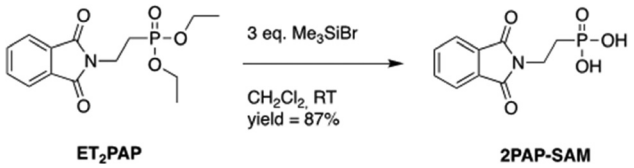

Fig. 3 Synthetic pathway to **2PAP-SAM**.

molecule LUMO level set to 4.10 eV[35] (Fig. 2f) compared to unfunctionalized ITO. Control samples were also prepared with ITO immersed in a control solution of THF without **2PAP-SAM**. For all immersion times, the control samples only showed a slight decrease down to 4.8 eV (Fig. 2a), attributed to the removal of hydroxide groups and presence of THF molecules adsorbed on the surface. For spincoating, a solution of 1 mM in THF of **2PAP-SAM** and 3.59 mM (1 mg mL^{-1}) in THF of **IC-SAM** was also prepared and deposited onto ITO substrates that were thermally annealed and rinsed in the same way as for the immersed substrates. The work functions of the samples were also measured by Kelvin probe analysis, and one can observe that both SAMs shift the work function of ITO to 4.35 and 4.43 eV, respectively. This reduction was correlated with the molecular dipole of both **2PAP-SAM** and **IC-SAM**, as shown in Fig. 1b, and notably the difference in work function between the substrates is directly related to the difference in the molecular dipole, as illustrated in Fig. S9.

The contact angle and surface energy, including polar and dispersive components, were also measured and calculated using the standard Owens, Wendt, Rabel and Kaelble (OWRK) method[36–40] for the different immersion times as well as for the spincoated samples (Fig. 2b and Table S1). A significant decrease from high hydrophilicity (mean contact angle of 14° with water) and a surface energy above 80 mN m^{-1} to a contact angle with water of 47° and a surface energy of 55 mN m^{-1} is observed after only one hour of immersion. For longer immersion times, the surface energy reaches a minimum at 44 mN m^{-1} after 24 h and slowly increases back to 52 mN m^{-1} after 70 h, while the contact angle with water stays at around 50° for all experiments. The spincoated samples also present a contact angle with water of around 50° for both SAMs and a surface energy of 49 mN m^{-1} for **2PAP-SAM** substrates, similar to the value for substrates immersed for 16 hours. For the **IC-SAM** samples, the surface energy value is slightly higher at 52 mN m^{-1}.

Table 1 shows the measurements of the contact angle and calculation of the surface free energy for 5 batches of ZnO, ITO, optimised **2PAP-SAM** (immersed for 24 hour or spincoated) and **IC-SAM** samples. One can first notice that the two methods of grafting of **2PAP-SAM**, immersion and spincoating, lead to very similar values of surface energy, contact angles and WF, suggesting that both methods are well adapted for functionalising the ITO. Moreover, the decrease of hydrophilicity and in surface energy between ITO and SAM grafted ITO is again observed for both SAMs, with the **IC-SAM** presenting a slightly higher value of 55 mN m^{-1}, while zinc oxide samples present a surface energy value closer to that of ITO with the polar component being the dominant one.

As such, the reduction observed for the SAM samples is directly linked to the decrease of the polar component and the slight increase of the dispersive component of the total surface free energy, especially in the case of the **2PAP-SAM** samples. The lower surface energy of the functionalised ITO with **2PAP-SAM** should allow better wettability between apolar organic materials solubilised in the fully dispersive solvent, chloroform (27 mN m^{-1})[38] and the substrate compared to pristine cleaned polar ITO by getting closer to the value of the surface energy of the active layer film and contribute to a more homogenous deposition of the active layer during spincoating.[41]

Ultraviolet photoelectron spectroscopy (UPS) was performed to complement and support the KP measurement. Special attention was given to ensure proper electrical contact between the sample and holder to prevent the charge effect from altering the measurement. Work function values determined by UPS of ITO, ZnO, **2PAP-SAM** and **IC-SAM** are presented in Table S2. One can observe in Fig. S10 that, similar to in KP measurements, **2PAP-SAM** efficiently decreases the WF of ITO, shifting it from 4.65 eV to 3.7 eV for spincoated **2PAP-SAM**. On the other hand, **IC-SAM** only decreases it down to 4.00 eV. These results validate the measurement performed with the KP set-up as well as the calculation of the dipole strengths. A small deviation can be observed between the WF measured by UPS and KP, which is usually found when comparing both techniques.[42–44] This difference can be due to the environment under which the experiment was performed: ultra-high vacuum for UPS, air for KP.

XPS measurement of pristine ITO, and spincoated and immersed **2PAP-SAM** under optimised conditions (concentration of 1 mM for both techniques and 24 h of immersion) was carried out to confirm the chemisorption of the phosphonic acid moiety. Fig. 2d shows an increase of the atomic mean percentage of phosphorus atoms at the surface, serving as the

Table 1 Contact angle, surface energy and work function of ZnO, cleaned ITO, spincoated and immersed **2PAP-SAM**, spincoated **IC-SAM** and the active material **PTQ10**:**Y6** film

Electron transport layer	Contact angle with water (°)	Surface free energy (mN m^{-1})	Dispersive component (mN m^{-1})	Polar component (mN m^{-1})	Work function (eV)
ZnO	**41** ± 11	**67** ± 12	**1.8** ± 0.8	**65** ± 13	**4.36** ± 0.05
No ETL (ITO)	**13** ± 2	**86** ± 1	**1.8** ± 0.2	**84** ± 1	**4.95** ± 0.15
Spincoated **2PAP-SAM**	**53** ± 3	**48** ± 3	**9.4** ± 2.5	**38** ± 4	**4.23** ± 0.08
Immersed **2PAP-SAM** (24 h)	**55** ± 7	**46** ± 2	**8.6** ± 1.8	**38** ± 7	**4.30** ± 0.10
Spincoated **IC-SAM**	**50** ± 4	**56** ± 6	**3.6** ± 1.3	**53** ± 6	**4.49** ± 0.04
PTQ10/**Y6** film	**104** ± 1	**27** ± 0.5	**27.1** ± 0.6	**0.2** ± 0.2	**4.44** ± 0.25

first proof of **2PAP-SAM** presence on the surface. The deconvolution of the O 1s core level peak revealed, on the one hand, a decrease of the peak attributed to In–O and Sn–O at 530.2 eV due to coverage by the aromatic moiety and, on the other hand, the presence of specific peaks attributed to **2PAP-SAM** as well as its covalent grafting on ITO. In particular, one can detect the presence of peaks related to In–O–P and In···O═P at 531.2 eV[45,46] and C═O attributed to N–C═O at 532.2 eV.[47] These different observations confirm chemical bonding for both SAM deposition techniques onto the ITO substrate.

Ider to evaluate the homogeneity of the surface functionalisation with **2PAP-SAM**, Kelvin probe force microscopy (KPFM) measurement was also carried out. Fig. S12 confirms the decrease of the work function after surface modification with **2PAP-SAM**, starting from 5.08 ± 0.13 eV for ITO, and going to 4.39 ± 0.13 eV for ZnO, 4.90 ± 0.02 eV for **IC-SAM**, and 4.33 ± 0.11 and 4.41 ± 0.01 eV for spincoated and immersed **2PAP-SAM**, respectively. Although the immersion method leads to an efficient decrease of the WF, the samples present inhomogeneity on the surface, with aggregates of SAM localised at some parts of the surface. Topographic atomic force microscopy (AFM) imaging was also carried out on the same samples and the root-mean-square (RMS) roughness of the different surfaces was analysed. For ITO with **2PAP-SAM** prepared by immersion, the extracted roughness value of 4.6 nm appeared higher than that of ITO with **2PAP-SAM** prepared by spincoating, which was only 4.0 nm. In addition, aggregates are also observable on the topographic image (Fig. S12), confirming the higher inhomogeneity for the grafting when using the immersion method. The ITO, ZnO and **IC-SAM** samples presented low RMS roughness of 3.9, 2.7 and 3.8 nm, respectively. Overall, apart from the immersion samples, ITO and ITO covered with SAMs present comparable roughness values, and only ZnO appears to smoothen the surface.

To better understand how **2PAP-SAM** can interact with the ITO surface and change its properties, the adsorption of this molecule on a 4 × 4 periodic surface deficient of oxygen was computed at the DFT level. It was observed that adsorption occurs through the phosphonate moiety with the formation of 3 In–O bonds that anchor the molecule strongly on the surface using 3 of the 16 possible metal sites. Since the total dipole moment of a periodic surface is not unique, the focus was set on the variation of the z-component of the surface dipole Δp that can be directly linked to the surface work function change ΔW by the relationship

$$\frac{\Delta p}{S_0 \varepsilon} = \Delta W$$

with S the slab surface and ε_0 the vacuum permittivity.[48] Δp is evaluated to 1.1 D for the adsorption of one **2PAP-SAM** over a surface of 207 Å^2. This surface dipole change is 3 times smaller than the **2PAP-SAM** molecule dipole.

Nevertheless, if we consider a surface saturated at around 0.2 **2PAP-SAM**/Å^2 the extrapolated ΔW reaches around 0.8 eV, which is close to the 0.7 observed experimentally, making the computed value believable. Investigation of why a lower dipole is observed for the adsorbed molecule leads us to note that the dipole moment is tilted relative to the perpendicular direction, making it less efficient to shift the potential, reducing the effective surface dipole. Moreover, computing the charge reorganization upon adsorption, as presented in Fig. 4, shows that a fraction of an electron is transferred from the surface to the upper positive part of the molecule (mostly at the oxygen atoms and the phenyl ring), reducing the local positive charge and the dipole intensity. Therefore, not only should the intrinsic dipole of the free SAM molecule be considered, but also the adsorbed molecule orientation relative to the surface and the charge transfer with the surface that modifies the efficiency of the molecule to modify the work function change of the surface.

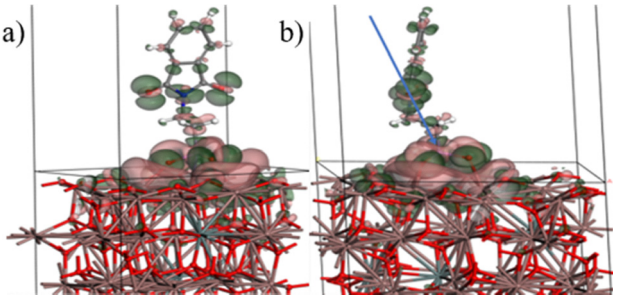

Fig. 4 **2PAP-SAM** adsorbed on the ITO (111) surface. The green and pink isosurfaces show the electron density variation upon adsorption on the surface. Green isosurfaces corresponds to electron accumulation while pink to electron reduction. The blue arrow shows the direction of the molecular dipole.

2.3. Integration of 2PAP-SAM as an electron selective layer in an OPV device

Since **2PAP-SAM** was confirmed to successfully create a covalent bond with ITO, and shift the work function towards more favourable values, OPV devices were prepared with an inverted (n–i–p) architecture and compared to ZnO, no ETL (ITO), spincoated and immersed **2PAP-SAM** and **IC-SAM** as ETLs. **PTQ10**:**Y6** in a ratio of 1:1.2 was chosen as the organic active material blend as a trade-off between performance and stability, reaching a PCE of up to 16.5% with a direct structure[49] and a PCE of 11.9% with an inverted structure and **IC-SAM** on top of ZnO.[50] **PTQ10** (Fig. 1e), while being an efficient and low cost material,[35] has been proven to be more stable than PM6, D18 or other polymer donors presenting a BDT-thiophene motif, demonstrated to be directly linked to rapid light induced degradation processes.[12,20] **Y6** (Fig. 1f), being part of the well-known and efficient NFA Y-family, is also reported to present good photostability in an inert environment.[17] Molybdenum trioxide (MoO_3) and silver as a hole transport layer and top electrode, respectively, complete the cell architecture.

OPV devices were first optimised in order to reach a sufficiently thick active layer together with high performance. Thin active layers (<100 nm) lead to a poor yield in the fabrication in particular for devices without ZnO on ITO, probably due to pinholes and defects resulting in short circuiting and thus unworkable devices. Hence, several ZnO reference cells were

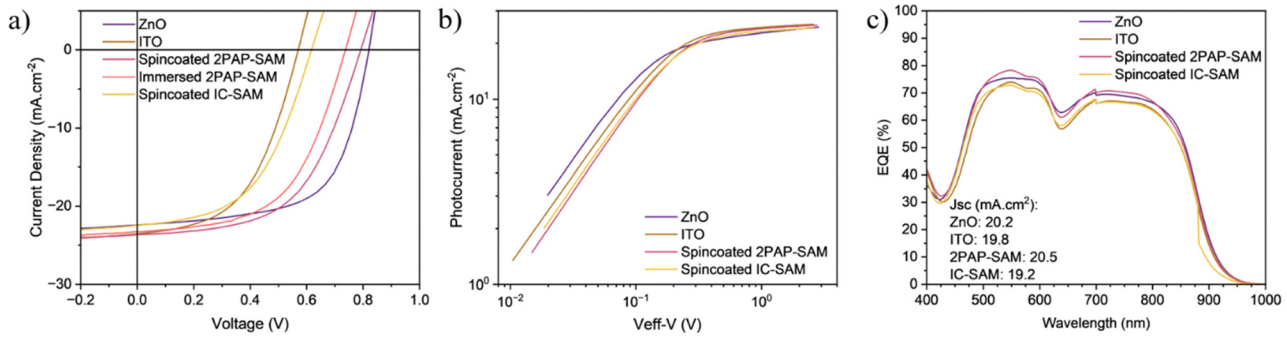

Fig. 5 (a) Current density–voltage curves of solar cells with different ETLs, (b) photocurrent-effective voltage curves of solar cells with different ETLs, and (c) EQE spectra of solar cells with different ETLs.

produced, varying the active material concentration and spincoating rotation speed in order to screen a large range of thicknesses, from 80 to 270 nm (Fig. S14 and S15). A trade-off was found for 130 nm, for which the performance remains high while maintaining a high yield for device fabrication for both ZnO and ZnO free cells.

The current density–voltage (J–V) curves of the different devices fabricated (ZnO, no ETL, immersed for 24 h in **2PAP-SAM** solution, spincoating of **2PAP-SAM** and **IC-SAM** solution) are presented in Fig. 5a, and all photovoltaic parameters are listed in Table 2. ZnO reference devices present PCEs of greater than 11.5% with an open circuit voltage (V_{OC}) of 0.82 V, similar to what can be expected from the literature for this blend, with this architecture, thickness and cell size.[51] Devices with spincoated **2PAP-SAM** as an ETL manage to achieve a PCE of 10% with V_{OC} up to 0.79 V, close to the values of the ZnO reference. With the immersion method (immersed **2PAP-SAM**), the device performance is slightly lower, mainly due to a smaller V_{OC} value of 0.73 V. In addition, in accordance with AFM measurement, the immersion strategy as a means to obtain a functionalised ITO electrode leads to more dispersed results and reproducibility issues, with only 6 out of 12 working devices compared to spincoated **2PAP-SAM** OPV devices with 12 out of 12 working devices (Table 2). This phenomenon was observed in several batches, as shown in Fig. S16, with only on average 2 out of 3 working devices for immersed samples, and among the working ones, low R_{shunt} values were observed (between 40 and 400 kΩ compared to 300 to 80 000 kΩ for spincoating and 300 to 17 000 kΩ for ITO alone), confirming the impact of deposition *via* immersion on the appearance of pinholes and increase of leakage current. Moreover, due to the varying thickness of the SAM for immersed devices, an S-shape in the IV curves was observed among working immersed devices even for low immersion times, indicating this grafting method to be too haphazard. ITO devices, on the other hand, show only a poor performance with the PCE lower than 7% and V_{OC} around 0.5 V, even with spincoating of THF onto cleaned ITO, producing a similar performance, confirming that **2PAP-SAM** has a distinct specific effect on devices not ascribable to cleaned ITO alone. **IC-SAM** devices manage to perform slightly better thanks to an increase of V_{OC} up to 0.61 V, without reaching the performance of **2PAP-SAM**. Moreover, **IC-SAM** cells also suffer from reproducibility issues, attributed in this case to the weaker binding strength of carboxylic acid with ITO in comparison to phosphonic acids[33] shown with the number of operational devices in Table 2 and Fig. S16. The results obtained with **2PAP-SAM**, and especially the increase of V_{OC} compared to bare ITO, can be correlated with the work function modification due to the molecular dipole of the **2PAP-SAM** molecule, as the Fermi level of the modified ITO electrode matches the acceptor LUMO level.

The impact of the concentration of the **2PAP-SAM** solution (from 0.1 to 2 mg mL^{-1}) on the performance of the OPV devices was also investigated. The evolution of the photovoltaic parameters as a function of the **2PAP-SAM** concentration is shown in Fig. S17. No significant variation is observed for the different concentrations for all parameters, suggesting that the **2PAP-SAM** layer formed on the ITO is always of the same length. This result also confirms that the cleaning protocol successfully removes excess **2PAP-SAM** molecules, and corroborates homogeneous surface modification even for low **2PAP-SAM** concentrations.

The photocurrent *versus* effective voltage is plotted in Fig. 5b to determine charge collection and dissociation probabilities.[28,52,53] For the latter, values of 92 ± 2% for ZnO, ITO and **IC-SAM** conditions and 94.4 ± 0.4% for **2PAP-SAM** were obtained, with

Table 2 The main parameters of organic solar cell devices measured under illumination of AM 1.5G (100 mW cm^{-2})

Electron transport layer	J_{SC} (mA cm^{-2})	V_{OC} (V)	FF	PCE (%)	Working devices
ZnO	**22.8** ± 0.3	**0.82** ± 0.01	**0.61** ± 0.02	**11.6** ± 0.3	9/12
No ETL (ITO)	**23.5** ± 0.1	**0.56** ± 0.04	**0.51** ± 0.02	**6.7** ± 0.7	3/4
Spin coated **2PAP-SAM**	**23.8** ± 0.5	**0.79** ± 0.00	**0.56** ± 0.03	**10.4** ± 0.4	12/12
Immersed **2PAP-SAM** (24 h)	**23.5** ± 0.5	**0.73** ± 0.01	**0.55** ± 0.01	**9.5** ± 0.3	6/12
Spin coated **IC-SAM**	**22.0** ± 0.7	**0.61** ± 0.04	**0.51** ± 0.03	**6.9** ± 0.7	7/12

comparable values being mostly dependent on the use of the same active material blend. On the other hand, a more pronounced difference is observed for charge collection. For ITO and **IC-SAM** the probability is only 67 ± 4%, while for ZnO, it is around 73 ± 3%, and for **2PAP-SAM** around 76 ± 1%. This slightly greater value for **2PAP-SAM** confirms that the charge collection properties are comparable with those of ZnO. Conversely, we do not observe a significant change in current density (J_{SC}) between all conditions, as shown in Table 2 and Fig. 5(c).

This work also explored the use of **2PAP-SAM** to passivate the ZnO ETL layer and compared to **IC-SAM** in this paradigm. The photovoltaics parameters were slightly improved compared to ZnO-based devices as shown in Fig. S18 and Table S3, with the PCE reaching up to 11.3% (average), but the impact of the passivation was more easily observed in stability measurements.

2.4. Stability and photo oxidation measurement

Finally, stability studies in a dark and protected environment (ISOS-D-1) or under continuous light illumination (ISOS-L-1) were performed.[54] First, for the ISOS-D-1 protocol, cells were kept in the dark in a nitrogen filled glovebox, and then measured periodically. Storage in the dark shows that even with sporadic illumination during measurement, the ZnO cell performance slowly decrease over time, leading to a PCE of 9% after 20 days, corresponding to 18% total loss (Fig. S19). This loss of performance is linked to a decrease of 10% of the fill factor, coupled with a 7% loss of J_{SC} (Fig. S20). In comparison, ZnO-free devices (bare ITO, **IC-SAM** and **2PAP-SAM**) show relatively stable FF over time and a much smaller loss of current density. Moreover, while ZnO cells maintain a constant V_{OC}, **2PAP-SAM**, **IC-SAM** and bare ITO devices show a general increase. For **2PAP-SAM** devices, the open circuit voltage increases from 0.76 V to 0.79 V after one night and remains constant upon storage. OPV devices with bare ITO show a steady increase, going from 0.54 to 0.63 V, improving therefore at the same time the PCE. This increase of the V_{OC} is also observed with **IC-SAM** cells that follow the same trend as OPV devices with only ITO. Overall, this experiment shows that even without continuous UV light excitation, ZnO seems to interact with the active layer and degrade it permanently, affecting cell performance, while ZnO-free devices retain a steady performance.

For stability under light, the ISOS-L-1 protocol was followed with encapsulated cells under a maximum power point (MPP) tracking load and submitted to 100 mW cm^{-2} constant illumination at a controlled temperature of 50 °C with (Fig. 6c) or without (Fig. 6d) a UV filter with a 400-nm cut-off. It is shown in Fig. 6c that all conditions present a strong burn-in effect in the first 20 minutes, most probably due to in-bulk degradations.[20,55,56] This burn-in effect is even stronger in the presence of UV light, as shown in Fig. 6d. Nevertheless, it appears that all ZnO-free OPV devices reach a stable performance faster and retain higher performances than ZnO-based OPV devices, with and without UV light in the spectrum. Indeed, the performance of ZnO drops to 40% of the initial performance without UV light and to 20% with UV light, whereas cells with **2PAP-SAM**, **IC-SAM** or bare ITO maintained more than 50% of the performance, no matter what spectrum was used, with 65% of the

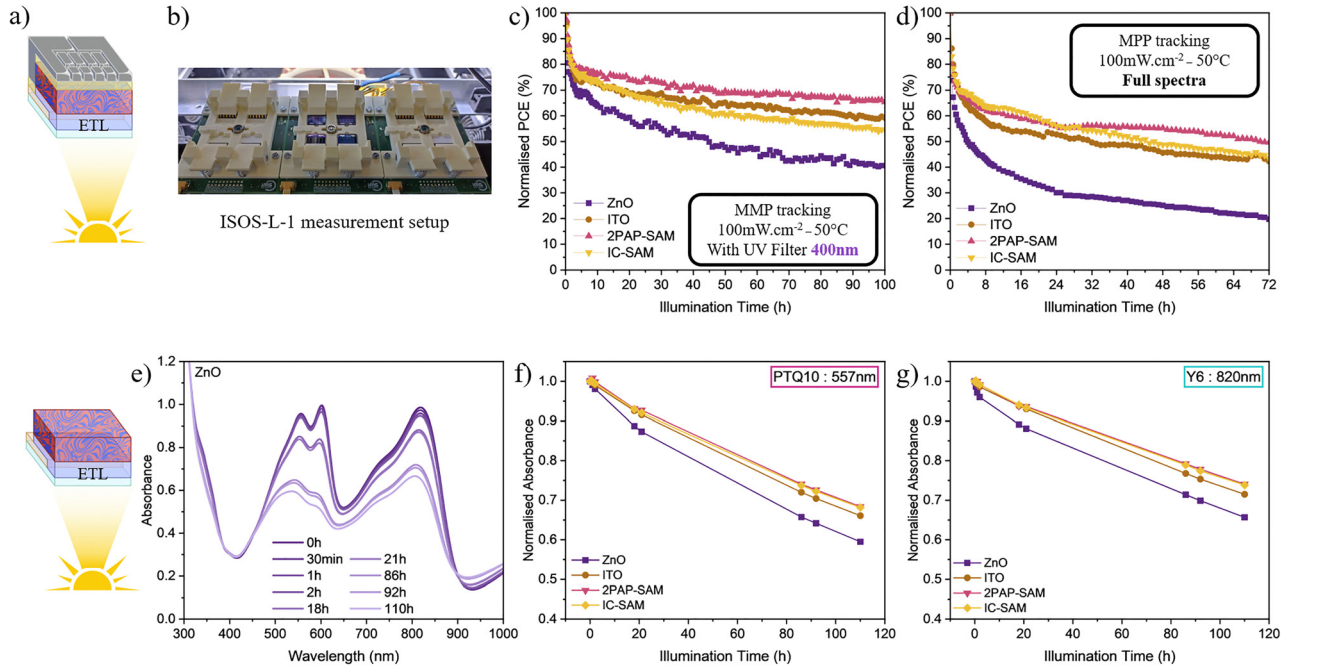

Fig. 6 (a) Schematics showing stability and photo oxidation measurement, (b) picture of the ISOS-L-1 setup, (c) evolution of the PCE under continuous illumination with MPP load with a UV filter at 400 nm, (d) evolution of the PCE under continuous illumination with MPP load without a UV filter, (e) evolution of the absorbance of the **PTQ10**:**Y6** film cast onto ZnO under continuous illumination in air, (f) evolution of the normalised absorbance for the main peak of **PTQ10**, and (g) evolution of the normalised absorbance for the main peak of **Y6**.

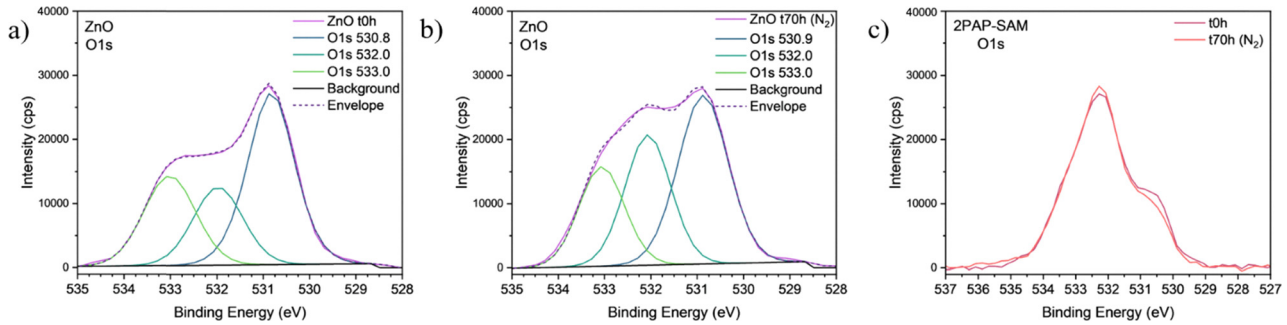

Fig. 7 XPS measurements showing O1s orbital spectra with deconvolution of the main peak contributions (LA model) of the ZnO substrate (a) before, and (b) after 72 h of 1 sun illumination in a protected environment, and (c) XPS measurements showing O1s orbital spectra of **2PAP-SAM** substrates before and after 72 h of 1 sun illumination in a protected environment.

initial performance being safeguarded without UV light. After 72 h of illumination with UV light, ZnO + SAM devices, with both **IC-SAM** and **2PAP-SAM**, manage to safeguard 50% of the initial performance while devices with bare ZnO lose 80% of the efficiency. Compared to ZnO, the addition of the SAM allows the preservation of the J_{SC} and FF to the same level as ITO devices (Fig. S18). Overall, between ZnO and ZnO-free devices, this difference in performance loss is mainly due to a significant drop of the V_{OC} (Fig. S20) for ZnO cells as it decreases to 0.55 ± 0.01 V after 72 h of ageing, a value below those of OPV devices with ITO (0.58 ± 0.02 V), **IC-SAM** (0.59 ± 0.02 V) and **2PAP-SAM** (0.61 ± 0.01 V).

To summarise, combining the normalised values with initial performances, **2PAP-SAM** stands out as a more stable alternative than ZnO as an ETL material. This difference in stability is attributed to the interaction between ZnO and the organic active layer and photodegradation that arises, which deteriorate the active layer at the interface. In contrast, ZnO-free substrates do not show this kind of degradation mechanism. To confirm this phenomenon, the evolution of the UV-visible spectra of different **PTQ10:Y6** films deposited on different ETLs (bare ITO, spincoated **2PAP-SAM**, **IC-SAM**, and ZnO) upon ageing in air (100 mW cm^{-2}, 50 °C) were studied. As shown in Fig. S22 and Fig. 6e, for an active layer cast onto ZnO, the absorbance of the active materials decreases over time, illustrating the degradation of the organic molecule mostly by a photo oxidation mechanism. By following the **PTQ10** and **Y6** main absorption peaks over time, one can observe faster degradation of the active materials deposited onto ZnO, as shown in Fig. 6f and g and Fig. S23, as already reported by Zhou *et al.*[17] These results highlight that under photo-oxidation, ZnO induces an additional degradation mechanism, most probably occurring at the interface with the active layer. Additionally, while looking at the evolution of the absorbance for the ZnO + SAM substrate aged under the same conditions, an intermediate rate of degradation is observed, confirming the active role of ZnO as the main cause for intrinsic degradation in the stack of layers and the necessity to remove it.

Additional proof can be obtained using XPS analysis of a thin active layer of the material **PTQ10:Y6** ($\sim$7 nm) cast onto an ITO + ZnO or ITO + **2PAP-SAM** substrate, and making comparisons before and after 70 h of 1 sun illumination. As for the device characterisation, this experiment took place inside a glove box as a protective environment in order to eliminate the extrinsic degradation caused by external O_2 and humidity. As illustrated in Fig. S24, a general survey for both conditions confirms that all layers are probed, with visible signals attributed to ZnO (especially Zn $2p_{3/2}$ and Zn $2p_{1/2}$ separated by 23 eV)[47,55,57–60] and ITO[47,59–61] layers. XPS measurement for the C 1s orbital and deconvolution is presented in Fig. S24 for all conditions, but this does not show any quantifiable change after illumination. Further, as illustrated in Fig. 7, a study of O 1s orbital spectra gives more information. For the ZnO substrate, deconvolution showed contributions from C═O bonds in the active layer materials at 533 eV, while contributions at 530.8 and 532 eV arise from oxygen present in the lattice of the oxide and from hydroxide or defects/vacancies usually present at the surface, respectively. When comparing ZnO samples before and after illumination, a striking increase of the defect contribution peak intensity (532 eV) can be observed, with the other peak intensities remaining similar. This evolution can be interpreted as a result of a photoinduced phenomenon leading to an increase of the reactivity of the ZnO interface.[62] On the other hand, **2PAP-SAM** substrate O1s orbital analysis does not show significant change after illumination, confirming that ITO + **2PAP-SAM** represents an inert surface. One can also note that the Zn $2p_{3/2}$ peak is shifted and has a greater FWHM (from 1.55 to 1.73), confirming a change to the lattice of ZnO (Fig. S26).

This supressed interfacial degradation mechanism for ZnO-free samples (bare ITO, **2PAP-SAM** and **IC-SAM**) is the main explanation for the improved stability observed in the devices.

3. Conclusions

In conclusion, this study outlines the possibility of improving the stability of inverted organic solar cells by replacing the ZnO ETL by a well-designed molecule such as **2PAP-SAM**. It was shown that the molecule can successfully bind to ITO reproducibly *via* spincoating deposition and a thorough cleaning protocol. **2PAP-SAM** acts as a suitable ETL material as a consequence of its molecular dipole shifting the work function of

the ITO electrode from 5.05 eV to 4.23 eV, better matching the **Y6** acceptor molecule LUMO level. Its integration in devices with a **PTQ10:Y6** blend was successfully optimised to obtain a reproducible protocol and excellent overall performance. **2PAP-SAM** devices are able to exhibit a PCE of 10%, compared to a PCE of 11.5% for ZnO reference devices, mainly due to an increase of the V_{OC} from 0.56 V for a pristine ITO device to 0.79 V, and charge collection capabilities comparable to ZnO cells. Meanwhile, devices using **IC-SAM**, a common SAM usually grafted onto ZnO, only achieved an increase in the V_{OC} up to 0.61 V. This difference is due to a lower molecular dipole and smaller work function shift (4.49 eV). ZnO-free devices were then proved to be more stable during dark storage and in operation under the ISOS-L-1 protocol and photo oxidation study, because of the apparent absence of photocatalytic activity, allowing **2PAP-SAM** devices to retain 65% of their performance after 100 h of 1 sun illumination with a UV filter, while ZnO devices could only retain 40% of the PCE. From these first results, we can conclude that **2PAP-SAM** can be successfully integrated into inverted devices as a promising candidate for an electron transport layer material, as a substitute for ZnO, to produce ZnO-free solar cells, allowing many opportunities for optimisation.

4. Experimental

3.1. Materials

[Poly[(thiophene)-*alt*-(6,7-difluoro-2-(2-hexyldecyloxy)quinoxaline)]] (**PTQ10**) and [2,2′-((2Z,2′Z)-((12,13-bis(2-ethylhexyl)-3,9-diundecyl-12,13-dihydro-[1,2,5]thiadiazolo[3,4*e*]thieno[2″,3″:4′,5′]thieno[2′,3′:4,5]pyrrolo[3,2*g*]thieno[2′,3′:4,5]thieno[3,2-*b*]indole-2,10-diyl)bis(methanylylidene))-bis(5,6-difluoro-3-oxo-2,3-dihydro-1*H*-indene-2,1-diylidene))dimalononitrile] (BTP-4F or **Y6**) were purchased from Brillant Matters. [Diethyl(1,3-dioxoisoindolin-2-yl)ethylphosphonate] (**Et$_2$PAP**) was purchased from BLDpharm and bromotrimethylsilane (Me_3SiBr) from Sigma Aldrich. [4-((1,3-dioxo-1,3-dihydro-2*H*-inden-2-ylidene)methyl)-benzoic acid] (**IC-SAM**) was obtained from abcr GmbH. All solvents and chemicals were used as received.

3.2. Device fabrication

OPV devices were fabricated with the inverted (n–i–p) architecture glass/ITO/ETL/active layer/MoO_3/silver. Glass ITO substrates (15 × 15 × 0.7 mm, 10 Ω $\square^{-1}$ resistance, 250-nm thick from visionTek) were first cleaned using an ultrasonic bath in different solvents: with 2%$_v$ HellmanexIII solution, deionized water (10 MΩ), acetone and isopropanol followed by 15 min of UV-O_3 treatment before ETL deposition or storage in an inert environment before active layer deposition for no-ETL devices.

For reference ZnO devices, a 0.15 mol L^{-1} solution of zinc acetate dihydrate (>99.0% from SigmaAldrich) with ethanolamine (>99.8 from SigmaAldrich) in a 1:1 molar ratio in absolute ethanol (>99.8% from SigmaAldrich) was prepared and stirred for 30 min at 55 °C, then aged overnight. Deposition was carried out after filtration by static spincoating (2000 rpm, 600 rpm s^{-1} acceleration, 60 s, 40 μL), then substrates were annealed at 180 °C (Fig. S6) for 30 min to create a 30-nm film and stored in an inert environment.

For SAM based devices, a 1 mmol L^{-1} (or 0.255 mg mL^{-1}) solution of **2PAP-SAM** in THF (inhibitor-free (>99.9%) from SigmaAldrich) or a 1 mg mL^{-1} solution of **IC-SAM** was prepared and stirred for 30 min at 50 °C, then sonicated for 2 min before filtration and deposition at ambient temperature. Deposition was carried out either by immersion in a 1 mM solution of **2PAP-SAM** in THF or by static spincoating (3000 rpm, 1000 rpm s^{-1} acceleration, 50 s, 40 μL). Substrates were then annealed for 10 min at 100 °C to promote the condensation of phosphonic acid with ITO. After annealing, substrates were placed in isopropanol/$THF_{20\%v}$ solution for a 15 min sonication bath to thoroughly wash all unbonded molecules, then dried again on a hot plate at 100 °C for 5 min before storage in an inert environment (Fig. 1d).

The organic active layer solution was prepared with **PTQ10:Y6** in a 1:1.2 wt ratio, at a 20 mg mL^{-1} concentration in anhydrous chloroform (>99.8 from SigmaAldrich), with stirring overnight at 55 °C. Deposition was carried out by dynamic spincoating (1100 rpm, 600 rpm s^{-1} acceleration, 60 s, 35 μL), then annealing at 100 °C for 10 min. Finally, 7 nm of MoO_3 as a HTL and 70 nm of a silver top electrode were then deposited by thermal evaporation to obtain 10.5 mm^2 cells that were finally separated by a thin needle to be measured individually.

For characterisation outside a glovebox, cells were encapsulated with a thin glass slide fixed with a DeloLP655 UV glue cross-linked by 40 s UV exposure with a DeloLux Pilot A1T.

3.3. Characterisation

Contact angle and surface free energy measurement were carried out using the Theta Flex Attension Optical Tensiometer from Biolin Scientific by measuring the angle between air, the substrate and different solvents (water, ethylene glycol and diiodomethane) following the Owens, Wendt, Rabel and Kaelble (OWRK) method and using the geometric mean formula with deionised water (10 MΩ), ethylene glycol (from SigmaAldrich) and iodomethane (>99% stabilized by silver wire from Thermo Fisher Scientific).[37,39]

Kelvin probe measurement was carried out using Kelvin probe S and Kelvin Control 07 from Besocke Delta Phi inside a Faraday cage. Following the Lord Kelvin principle and Zisman system,[63] the apparatus consists of a gold grid electrode oscillating closely on top of a conductive substrate. The oscillation creates an alternative current that can be stalled by applying a backing potential, equal to the contact potential difference between the substrate and the gold grid. The work function of the substrate is then obtained by comparing the contact potential difference of a reference HOPG (ZYH grade from Neyco) to the one of the measured substrate.[64]

Ultraviolet photoelectron spectroscopy was performed with a PHOIBOS 100 hemispherical energy analyser fitted with a SPECS UVS 10/35 UV source and multi-channel detector. The sample was exposed to an excitation energy of 21.22 eV from a

He^{I} discharge lamp at a 45° incident angle and photoelectrons were collected normal to the sample surface. The analyser mode was set at low angular dispersion and pass energy at 10 eV. A bias voltage of −4 V was applied to emphasize the secondary-electron cut-off (SECO). Charge effects were ruled out using 3 scans at different bias voltages. Work function values were extracted by intercepting the linear regression of the SECO region and the baseline.[43]

X-ray photoelectron spectroscopy (XPS) was performed using a K-Alpha spectrometer (ThermoFisher Scientific) equipped with a monochromatic Al-Kα X-ray source (1486.6 eV). The X-ray spot was selected with a diameter of 400 μm. Survey scans were collected in the full energy range (0–1100 eV) at a pass energy of 200 eV, whereas high-resolution spectra were obtained at a pass energy of 40 eV. Quantification was carried out for areas of high-resolution spectra with Scofield sensitivity factors.

Solar cell characterisation was performed using a solar simulator (Newport LCS-100) with a xenon lamp and AM 1.5 G filters to measure the IV characteristics of the OPV devices. The total irradiance of the lamp was set at 100 mW cm^{-2} using a calibrated silicon reference cell from Newport Co. The *J–V* curves were recorded in a nitrogen-filled glovebox in the dark and under 1 sun using a Keithley 2400 SMU, from −2 V to +1 V with a step of 0.03 V and a source/measure delay of 0.001 s. The main parameters (resistances, J_{SC}, V_{OC}, FF and PCE) were directly extracted *via* the LabVIEW program. The active area was defined by the size of the top electrode evaporated (10.5 mm^2). No shadow masking was used.

External quantum efficiency measurements were carried out in an ambient atmosphere with encapsulated cells with a PVE 300 from Bentham Co calibrated with a silicon cell from 300 to 1000 nm with a 1-nm step.

UV-visible measurements were carried out using the UVmc^2 SAFAS Monaco from 300 to 1000 nm with a 1 nm step.

Photo oxidation measurement was carried out in an ambient atmosphere using a xenon test chamber model Xe-1 from Q Sun set at 0.47 W m^{-2} at 340 nm to obtain an irradiance of 100 mW cm^{-2} with a constant temperature of 50 °C.

Stability measurement was carried out using an HMI metal halide lamp with 100 mW cm^{-2} irradiance and 55 °C constant temperature with MPP tracking. *J–V* curves were recorded in ambient air with encapsulated cells with a step of 0.05 V and 0.08 s setpoint measure delay setpoint, following recommendation from the ISOS-L-1 protocol.[54]

3.4. Computational details

Periodic calculations were performed within the density functional theory (DFT) framework, using the Vienna *ab initio* simulation package (VASP).[65–67] The electronic wave functions have been expanded in a plane-wave basis set with a kinetic energy cut-off up to 500 eV. Projector augmented wave (PAW) pseudopotentials were used as implemented in VASP.[68,69] The exchange–correlation effects have been accounted for by the generalised gradient approximation (GGA) using the functional of Perdew, Burke and Ernzerhof (PBE).[70] In order to improve the description of the interaction between adsorbed molecules and the ITO surface, van der Waals dispersion interactions have been accounted for by using semi-empirical correction as proposed by Grimme *et al.* (PBE-D3).[71] A convergence criterion has been set to 1.10^{-5} eV for the electronic self-consistent iterations. The structural relaxation was performed until the maximum force on any atom was below 1.10–2 eV $Å^{-1}$. A Sn doped ITO surface was modelled from an In_2O_3 structure doped with 4.6% Sn and cleaved in the (111) direction with 4 metal layers. The calculations were performed on 4 × 4 supercells with half the bottom part of the slab frozen to bulk parameters and the upper part (where the molecules are adsorbed) let to optimize. A vacuum layer of 10 Å has been set in the z-direction. The associated k-point grid was set with a 3 × 3 × 1 automatic sampling mesh. Individual molecules were computed in a large 20 × 20 × 20 $Å^3$ unit cell to prevent periodic interactions. Dipoles were computed by direct integration of the computed charge density. For periodic surfaces, the surface dipole is difficult to obtain reliably, and thus the focus was on the dipole moment variation of the surface upon molecule adsorption, which is more interesting to compare with the intrinsic dipole moment of the molecule in the gas phase.

Author contributions

Chélia Zalani: conceptualization, investigation, methodology, resources, writing – original draft (lead). Gilles H. Roche: conceptualization. Olivier Dautel: conceptualization, resources (synthesis, lead), writing – original draft (supporting). Martial Leyney: resources (ISOS-L-1 measurement bench). Jean-Sébastien Filhol: resources (DFT calculation), writing – original draft (supporting). Roland Lefevre: resources (UPS set up). Christine Labrugère: resources (XPS measurement). Gilles Pecastaings: resources (KPFM measurement). Guillaume Wantz: funding acquisition, supervision (supporting), writing – review & editing. Sylvain Chambon: funding acquisition, conceptualization, supervision (lead), writing – review & editing.

Conflicts of interest

There are no conflicts to declare.

Data availability

The data supporting this article have been included in the manuscript and as part of the supplementary information (SI). Supplementary information contains the description of the synthesis of 2PAP-SAM, additional surface characterization (contact angle, Kelvin probe measurements, KPFM, AFM), XPS, UPS and UV-visible analysis, structures and dipoles moments of computed SAMs, photovoltaic performances of the organic solar cells and their stability evaluation under different ageing conditions. See DOI: https://doi.org/10.1039/d5tc03674g.

Acknowledgements

This work was supported by a public grant overseen by the French National Research Agency (ANR) as part of the ''Investissements d'avenir'' program (reference: ANR-10-EQPX-28-01/ Equipex ELORPrintTec).

Notes and references

1 D. Yue, P. Khatav, F. You and S. B. Darling, *Energy Environ. Sci.*, 2012, **5**(11), 9163.
2 N. Espinosa, R. García-Valverde, A. Urbina and F. C. Krebs, *Sol. Energy Mater. Sol. Cells*, 2011, **95**(5), 1293–1302.
3 L. Zhu, M. Zhang, J. Xu, C. Li, J. Yan and G. Zhou, *et al.*, *Nat. Mater.*, 2022, **21**(6), 656–663.
4 A. Karki, A. J. Gillett, R. H. Friend and T. Q. Nguyen, *Adv. Energy Mater.*, 2021, **11**(15), 2003441.
5 A. Armin, W. Li, O. J. Sandberg, Z. Xiao, L. Ding and J. Nelson, *et al.*, *Adv. Energy Mater.*, 2021, **11**(15), 2003570.
6 H. Chen, Y. Huang, R. Zhang, H. Mou, J. Ding and J. Zhou, *et al.*, *Nat. Mater.*, 2025, **24**, 444–453.
7 M. Du, N. Sun, H. Cheng, X. Liu, X. Yi and Q. Guo, *et al.*, *Angew. Chem., Int. Ed.*, 2025, **137**(49), e202515114.
8 R. Basu, F. Gumpert, J. Lohbreier, P. O. Morin, V. Vohra and Y. Liu, *et al.*, *Joule*, 2024, **8**(4), 970–978.
9 M. A. Green, E. D. Dunlop, M. Yoshita, N. Kopidakis, K. Bothe and G. Siefer, *et al.*, *Prog. Photovolt. Res. Appl.*, 2025, **33**(1), 3–15.
10 N. Grossiord, J. M. Kroon, R. Andriessen and P. W. M. Blom, *Org. Electron.*, 2012, **13**(3), 432–456.
11 H. Xu, J. Han, A. Sharma, S. H. K. Paleti, S. Hultmark and A. Yazmaciyan, *et al.*, *Adv. Mater.*, 2025, **37**(4), 2407119.
12 J. Han, H. Xu, S. H. K. Paleti, A. Sharma and D. Baran, *Chem. Soc. Rev.*, 2024, **53**(14), 7426–7454.
13 W. Greenbank, N. Rolston, E. Destouesse, G. Wantz, L. Hirsch and R. Dauskardt, *et al.*, *J. Mater. Chem. A*, 2017, **5**(6), 2911–2919.
14 S. K. Hau, H. L. Yip and A. K. Y. Jen, *Polym. Rev.*, 2010, **50**(4), 474–510.
15 Y. Jiang, L. Sun, F. Jiang, C. Xie, L. Hu and X. Dong, *et al.*, *Mater. Horiz.*, 2019, **6**(7), 1438–1443.
16 M. Günther, D. Blätte, A. L. Oechsle, S. S. Rivas, A. A. Yousefi Amin and P. Müller-Buschbaum, *et al.*, *ACS Appl. Mater. Interfaces*, 2021, **13**(16), 19072–19084.
17 B. Zhou, L. Wang, Y. Liu, C. Guo, D. Li and J. Cai, *et al.*, *Adv. Funct. Mater.*, 2022, **32**(43), 2206042.
18 S. Balasubramanian, M. Á. León-Luna, B. Romero, M. Madsen and V. Turkovic, *ACS Appl. Mater. Interfaces*, 2023, **15**(33), 39647–39656.
19 S. Park and H. Jung Son, *J. Mater. Chem. A*, 2019, **7**(45), 25830–25837.
20 Y. Wang, J. Luke, A. Privitera, N. Rolland, C. Labanti and G. Londi, *et al.*, *Joule*, 2023, **7**(4), 810–829.
21 Z. Liang, Q. Zhang, L. Jiang and G. Cao, *Energy Environ. Sci.*, 2015, **8**(12), 3442–3476.
22 Y. Li, C. Ji, Y. Qu, X. Huang, S. Hou and C. Li, *et al.*, *Adv. Mater.*, 2019, **31**(40), 1903173.
23 H. Liu, Z. Liu, S. Wang, J. Huang, H. Ju and Q. Chen, *et al.*, *Adv. Energy Mater.*, 2019, **9**(34), 1900887.
24 Y. Li, X. Huang, K. Ding, H. K. M. Sheriff, L. Ye and H. Liu, *et al.*, *Nat. Commun.*, 2021, **12**(1), 5419.
25 H. Xu, S. Anirudh and H. Jianhua, *et al.*, *Adv. Energy Mater.*, 2024, **14**(44), 2401262.
26 M. Liu, L. Bi, W. Jiang, Z. Zeng, S. W. Tsang and F. R. Lin, *et al.*, *Adv. Mater.*, 2023, **35**(46), 2304415.
27 A. Farag, *Evaporated Self-Assembled Monolayer Hole Transport Layers: Lossless Interfaces in p-i-n Perovskite Solar Cells*.
28 S. Guan, Y. Li, C. Xu, N. Yin, C. Xu and C. Wang, *et al.*, *Adv. Mater.*, 2024, **36**(25), 2400342.
29 Y. Lin, Y. Zhang, J. Zhang, M. Marcinskas, T. Malinauskas and A. Magomedov, *et al.*, *Adv. Energy Mater.*, 2022, **12**(45), 2202503.
30 Y. Lin, A. Magomedov, Y. Firdaus, D. Kaltsas, A. El-Labban and H. Faber, *et al.*, *ChemSusChem*, 2021, **14**(17), 3569–3578.
31 A. Al-Ashouri, A. Magomedov, M. Roß, M. Jošt, M. Talaikis and G. Chistiakova, *et al.*, *Energy Environ. Sci.*, 2019, **12**(11), 3356–3369.
32 S. Jeong, J. Oh, J. Park, Y. Cho, S. Jung and S. Lee, *et al.*, *ACS Energy Lett.*, 2024, **9**(8), 3771–3779.
33 S. P. Pujari, L. Scheres, A. T. M. Marcelis and H. Zuilhof, *Angew. Chem., Int. Ed.*, 2014, **53**(25), 6322–6356.
34 P. J. Hotchkiss, S. C. Jones, S. A. Paniagua, A. Sharma, B. Kippelen and N. R. Armstrong, *et al.*, *Acc. Chem. Res.*, 2012, **45**(3), 337–346.
35 C. Sun, F. Pan, H. Bin, J. Zhang, L. Xue and B. Qiu, *et al.*, *Nat. Commun.*, 2018, **9**(1), 743.
36 J. Yuan, Y. Zhang, L. Zhou, G. Zhang, H. L. Yip and T. K. Lau, *et al.*, *Joule*, 2019, **3**(4), 1140–1151.
37 K. X. Ma, C. H. Ho, F. Zhu and T. S. Chung, *Thin Solid Films*, 2000, **371**(1–2), 140–147.
38 C. J. Van Oss, *Interfacial Forces in Aqueous Media*, 2nd edn, CRC Press, Boca Raton, 2006, p. 456.
39 D. K. Owens and R. C. Wendt, *J. Appl. Polym. Sci.*, 1969, **13**(8), 1741–1747.
40 D. Bonn, J. Eggers, J. Indekeu, J. Meunier and E. Rolley, *Rev. Mod. Phys.*, 2009, **81**(2), 739–805.
41 R. J. Good, *J. Adhes. Sci. Technol.*, 1992, **6**(12), 1269–1302.
42 F. Zhang, S. H. Silver, N. K. Noel, F. Ullrich, B. P. Rand and A. Kahn, *Adv. Energy Mater.*, 2020, **10**(26), 1903252.
43 J. E. Whitten, Ultraviolet photoelectron spectroscopy: Practical aspects and best practices, *Appl. Surf. Sci. Adv.*, 2023, **13**, 100384.
44 J. E. Whitten, *Surf. Sci.*, 2003, **546**(2–3), 107–116.
45 P. B. Paramonov, S. A. Paniagua, P. J. Hotchkiss, S. C. Jones, N. R. Armstrong and S. R. Marder, *et al.*, *Chem. Mater.*, 2008, **20**(16), 5131–5133.
46 S. A. Paniagua, A. J. Giordano, O. L. Smith, S. Barlow, H. Li and N. R. Armstrong, *et al.*, *Chem. Rev.*, 2016, **116**(12), 7117–7158.

47 G. Beamson and D. Briggs, *High Resolution XPS of Organic Polymers: The Scienta ESCA300 Database*, Wiley, 1992.
48 M. Mamatkulov and J. S. Filhol, *Phys. Chem. Chem. Phys.*, 2011, **13**(17), 7675.
49 Y. Wu, Y. Zheng, H. Yang, C. Sun, Y. Dong and C. Cui, *et al.*, *Sci. China: Chem.*, 2020, **63**(2), 265–271.
50 S. Kongsabay, G. H. Roche, O. Dautel, V. Promarak and G. Wantz, *Adv. Photonics Res.*, 2025, **6**(4), 2400128.
51 S. Riera-Galindo, M. Sanz-Lleó, E. Gutiérrez-Fernández, N. Ramos, M. Mas-Torrent and J. Martín, *et al.*, *Small*, 2024, **20**(26), 2311735.
52 V. D. Mihailetchi, L. J. A. Koster, J. C. Hummelen and P. W. M. Blom, *Phys. Rev. Lett.*, 2004, **93**(21), 216601.
53 L. Onsager, *J. Chem. Phys.*, 1934, **2**(9), 599–615.
54 M. O. Reese, S. A. Gevorgyan, M. Jørgensen, E. Bundgaard, S. R. Kurtz and D. S. Ginley, *et al.*, *Sol. Energy Mater. Sol. Cells*, 2011, **95**(5), 1253–1267.
55 A. Tournebize, G. Mattana, T. Gorisse, A. Bousquet, G. Wantz and L. Hirsch, *et al.*, *ACS Appl. Mater. Interfaces*, 2017, **9**(39), 34131–34138.
56 T. Heumueller, T. M. Burke, W. R. Mateker, I. T. Sachs-Quintana, K. Vandewal and C. J. Brabec, *et al.*, *Adv. Energy Mater.*, 2015, **5**(14), 1500111.
57 M. C. Biesinger, L. W. M. Lau and A. R. Gerson, Smart RStC, *Appl. Surf. Sci.*, 2010, **257**(3), 887–898.
58 U. P. Gawai and B. N. Dole, *RSC Adv.*, 2017, **7**(59), 37402–37411.
59 *NIST Inorganic Crystal Structure Database (ICSD)*. Available from: https://data.nist.gov/pdr/lps/ark:/88434/mds2-2147.
60 G. Kerherve, W. S. J. Skinner, J. A. Hochhaus, A. Graf, D. J. Morgan and M. A. Isaacs, *et al.*, *Surf. Interface Anal.*, 2026, **58**(1), 54–65.
61 J. D. Henderson, L. Pearson, H. Y. Nie and M. C. Biesinger, *Surf. Interface Anal.*, 2025, **57**(1), 81–97.
62 A. Manor, E. A. Katz, T. Tromholt and F. C. Krebs, *Adv. Energy Mater.*, 2011, **1**(5), 836–843.
63 W. A. Zisman, *Rev. Sci. Instrum.*, 1932, **3**(7), 367–370.
64 W. Melitz, J. Shen, A. C. Kummel and S. Lee, *Surf. Sci. Rep.*, 2011, **66**(1), 1–27.
65 G. Kresse and J. Hafner, *Phys. Rev. B: Condens. Matter Mater. Phys.*, 1994, **49**(20), 14251–14269.
66 G. Kresse and J. Furthmüller, *Comput. Mater. Sci.*, 1996, **6**(1), 15–50.
67 G. Kresse and J. Furthmüller, *Phys. Rev. B: Condens. Matter Mater. Phys.*, 1996, **54**(16), 11169–11186.
68 G. Kresse and D. Joubert, *Phys. Rev. B: Condens. Matter Mater. Phys.*, 1999, **59**(3), 1758–1775.
69 P. E. Blöchl, *Phys. Rev. B: Condens. Matter Mater. Phys.*, 1994, **50**(24), 17953–17979.
70 J. P. Perdew, K. Burke and M. Ernzerhof, *Phys. Rev. Lett.*, 1996, **77**(18), 3865–3868.
71 S. Grimme, S. Ehrlich and L. Goerigk, *J. Comput. Chem.*, 2011, **32**(7), 1456–1465.